Science AAAS

Decoupled catalytic hydrogen evolution from a molecular metal oxide redox mediator in water splitting

Benjamin Rausch *et al.*
Science **345**, 1326 (2014);
DOI: 10.1126/science.1257443

(*20*). In a hollow lattice, the nodes are constrained only by the shell walls, which has a detrimental effect on strength and stiffness because load transfer at the nodes occurs via shell wall bending. This, together with the sharp angles between the tubes, leads to an uneven distribution of stress and induces large stress concentrations in the vicinity of the nodes (Fig. 1, B and E). Bending of the tubes also causes large deflections and additional ovalization at the nodes, which further increases the compliance and stress concentrations. In situ experiments and postcompression analysis revealed that most of the deformation is localized to the nodes (Figs. 2, D and E, and 3J), which implies that improving nodal strength is a critical factor in enhancing the scaling of strength and stiffness with density.

We demonstrated the creation of ultralight hollow ceramic nanolattices that absorb energy, recover after significant compression, and reach an untapped strength and stiffness material property space. This is achieved using high-strength ALD alumina engineered into a thin-walled nanolattice that is capable of deforming elastically via shell buckling. The ultralight ceramic nanolattices represent the concept of materials by design, where it is possible to transform a strong and dense brittle ceramic into a strong, ultralight, energy-absorbing, and recoverable metamaterial. These results serve to emphasize the critical connection between material microstructure, hierarchical architecture, and mechanical properties at relevant length scales.

REFERENCES AND NOTES

1. D. Jang, L. R. Meza, F. Greer, J. R. Greer, *Nat. Mater.* **12**, 893–898 (2013).
2. J. R. Greer, J. T. M. De Hosson, *Prog. Mater. Sci.* **56**, 654–724 (2011).
3. X. W. Gu, Z. Wu, Y.-W. Zhang, D. J. Srolovitz, J. R. Greer, *Nano Lett.* **13**, 5703–5709 (2013).
4. D. Z. Chen *et al.*, *Nano Lett.* **13**, 4462–4468 (2013).
5. J. Rys *et al.*, *Adv. Eng. Mater.* **16**, 889–896 (2014).
6. L. R. Meza, J. R. Greer, *J. Mater. Sci.* **49**, 2496–2508 (2014).
7. X. Zheng *et al.*, *Science* **344**, 1373–1377 (2014).
8. J. Bauer, S. Hengsbach, I. Tesari, R. Schwaiger, O. Kraft, *Proc. Natl. Acad. Sci. U.S.A.* **111**, 2453–2458 (2014).
9. A. G. Evans, *J. Am. Ceram. Soc.* **73**, 187–206 (1990).
10. I.-W. Chen, L. A. Xue, *J. Am. Ceram. Soc.* **73**, 2585–2609 (1990).
11. P. F. Becher, *J. Am. Ceram. Soc.* **74**, 255–269 (1991).
12. D. C. Hofmann *et al.*, *Nature* **451**, 1085–1089 (2008).
13. E. Munch *et al.*, *Science* **322**, 1516–1520 (2008).
14. J. C. Weaver *et al.*, *J. Struct. Biol.* **158**, 93–106 (2007).
15. C. E. Hamm *et al.*, *Nature* **421**, 841–843 (2003).
16. M. A. Meyers, J. McKittrick, P.-Y. Chen, *Science* **339**, 773–779 (2013).
17. L. J. Gibson, M. F. Ashby, *Cellular Solids: Structure and Properties* (Cambridge Univ. Press, Cambridge, ed. 2, 1999).
18. V. S. Deshpande, M. F. Ashby, N. A. Fleck, *Acta Mater.* **49**, 1035–1040 (2001).
19. S. Pellegrino, C. R. Calladine, *Int. J. Solids Struct.* **22**, 409–428 (1986).
20. V. S. Deshpande, N. A. Fleck, M. F. Ashby, *J. Mech. Phys. Solids* **49**, 1747–1769 (2001).
21. T. A. Schaedler *et al.*, *Science* **334**, 962–965 (2011).
22. L. C. Montemayor, L. R. Meza, J. R. Greer, *Adv. Eng. Mater.* **16**, 184–189 (2014).
23. See the supplementary materials.
24. M. D. Groner, F. H. Fabreguette, J. W. Elam, S. M. George, *Chem. Mater.* **16**, 639–645 (2004).
25. Y. K. Akimov, *Instrum. Exp. Tech.* **46**, 287–299 (2003).
26. L. Valdevit, A. J. Jacobsen, J. R. Greer, W. B. Carter, *J. Am. Ceram. Soc.* **94**, s15–s34 (2011).
27. M. Berdova *et al.*, *Acta Mater.* **66**, 370–377 (2014).
28. H. G. Allen, P. S. Bulson, *Background to Buckling* (McGraw-Hill, Berkshire, UK, 1980).
29. G. Ju, S. Kyriakides, *Int. J. Solids Struct.* **29**, 1143–1171 (1992).
30. A. Torrents, T. A. Schaedler, A. J. Jacobsen, W. B. Carter, L. Valdevit, *Acta Mater.* **60**, 3511–3523 (2012).
31. L. Valdevit, S. W. Godfrey, T. Schaedler, A. J. Jacobsen, W. B. Carter, *J. Mater. Res.* **28**, 2461–2473 (2013).
32. K. J. Maloney *et al.*, *APL Mater.* **1**, 022106 (2013).

ACKNOWLEDGMENTS

The authors gratefully acknowledge the financial support from the Defense Advanced Research Projects Agency under the Materials with Controlled Microstructure and Architecture program managed by J. Goldwasser (contract no. W91CRB-10-0305) and to the Institute for Collaborative Biotechnologies through grant W911NF-09-0001 from the U.S. Army Research Office. The content of the information does not necessarily reflect the position or the policy of the government, and no official endorsement should be inferred. The authors are grateful to the Kavli Nanoscience Institute at Caltech for the availability of critical cleanroom facilities, and to R. Liontas and C. Garland for TEM assistance. Part of this work was carried out in the Lewis Group facilities at Caltech.

SUPPLEMENTARY MATERIALS

www.sciencemag.org/content/345/6202/1322/suppl/DC1
Materials and Methods
Figs. S1 to S6
Table S1
Reference (*33*)
Movies S1 to S3

12 May 2014; accepted 11 August 2014
10.1126/science.1255908

WATER SPLITTING

Decoupled catalytic hydrogen evolution from a molecular metal oxide redox mediator in water splitting

Benjamin Rausch, Mark D. Symes, Greig Chisholm, Leroy Cronin*

The electrolysis of water using renewable energy inputs is being actively pursued as a route to sustainable hydrogen production. Here we introduce a recyclable redox mediator (silicotungstic acid) that enables the coupling of low-pressure production of oxygen via water oxidation to a separate, catalytic hydrogen production step outside the electrolyzer that requires no post-electrolysis energy input. This approach sidesteps the production of high-pressure gases inside the electrolytic cell (a major cause of membrane degradation) and essentially eliminates the hazardous issue of product gas crossover at the low current densities that characterize renewables-driven water-splitting devices. We demonstrated that a platinum-catalyzed system can produce pure hydrogen over 30 times faster than state-of-the-art proton exchange membrane electrolyzers at equivalent platinum loading.

Hydrogen is vital for the production of commodity chemicals such as ammonia and has great potential as a clean-burning fuel (*1*, *2*). However, currently around 95% (~15 trillion mol $year^{-1}$) of the world's supply of H_2 is obtained by reforming fossil fuels (*3*), a process that is both unsustainable and leads to a net increase in atmospheric CO_2 levels. Of the alternative methods for H_2 production that are not linked to fossil resources, the electrolysis of water stands out as a mature, scalable technology for which the only required inputs are water and energy (in the form of electricity) (*4*). Hence, if the energy source is renewable, H_2 can be produced sustainably from water using electrolysis (*5*, *6*).

Renewable energy inputs tend to be sporadic and fluctuating, and thus the systems that are developed to harness this energy and convert it to H_2 [such as proton exchange membrane electrolyzers (PEMEs) (*7*), solar-to-fuels systems (*8*), and artificial leaves (*9*)] must be able to deal with varying energy inputs effectively and have rapid startup times. At the low power loads that are characteristic of renewable power sources, the rate at which H_2 and O_2 are produced may in fact be slower than the rate at which these gases permeate the membrane (*10*). At the very least, this will severely affect the amount of hydrogen that can be harvested from such devices (*11*), and in extreme cases could give rise to hazardous O_2/H_2 mixtures. The PEME is the most mature technology cited for renewables-to-hydrogen conversion, but prevention of such gas crossover at low current densities remains a challenge. PEMEs use nontrivial amounts of precious metal catalysts and so tend to operate at high current densities (1 A cm^{-2} or above) and high pressure, where the cost of their components can be offset to some extent (*7*). However, these optimal conditions may be hard to maintain in all cases of renewables-driven electrolysis (for example, in small-scale facilities), where less-expensive and lower-power devices would therefore be beneficial. Meanwhile, the high-pressure and high-current-density conditions under which PEMEs work most effectively are also not without drawbacks: These conditions can also lead to gas crossover through the membrane, and the coexistence of H_2, O_2 and catalyst particles produces reactive oxygen species

WestCHEM, School of Chemistry, University of Glasgow, University Avenue, Glasgow G12 8QQ, UK.
*Corresponding author. E-mail: lee.cronin@glasgow.ac.uk

(ROS) that degrade the membrane and shorten its lifetime (*12*, *13*). There is thus a need to develop new electrolyzer systems that can prevent product gases from mixing over a range of current densities and that make more effective use of the precious metal catalysts they employ, in order to make renewables-to-hydrogen conversion both practically and economically more attractive.

Previously, we introduced the concept of the electron-coupled proton buffer (ECPB), which can act to decouple electrolytic H_2 and O_2 production, producing these gases at separate times (*14*, *15*). Here we describe a redox mediator that can be reversibly reduced in an electrolytic cell (as water is oxidized at the anode) and then transferred to a separate chamber for spontaneous catalytic H_2 evolution, without the need for additional energy input after reduction of the mediator (Fig. 1). This approach leads to a device architecture for electrolyzers that has several important advantages. First, it allows the electrochemical step to be performed at atmospheric pressure, while potentially permitting H_2 to be evolved at elevated pressure in a distinct compartment. Second, virtually no H_2 is produced in the electrolytic cell itself, which (taken with the feature above) obviates the need to purge H_2 from the anode side of the cell and could significantly reduce ROS-mediated membrane degradation and the possibility of explosive gas mixtures forming at low current densities or upon membrane failure. Third, H_2 evolution from such a system is no longer directly coupled to the rate of water oxidation, and thus the decoupled H_2 production step can be performed a rate per milligram of catalyst that is over 30 times faster than that for state-of-the-art PEMEs (movie S1). Finally, the hydrogen produced has the potential to have an inherently low O_2 content, both on account of its production in a separate chamber from water oxidation and by virtue of the fact that the reduced mediator reacts rapidly with O_2 in solution. This final point could render the H_2 produced suitable for applications requiring high-purity H_2 such as fuel cells (*16*) or the Haber-Bosch process (*17*), without the need for post-electrolysis purification or built-in recombination catalysts.

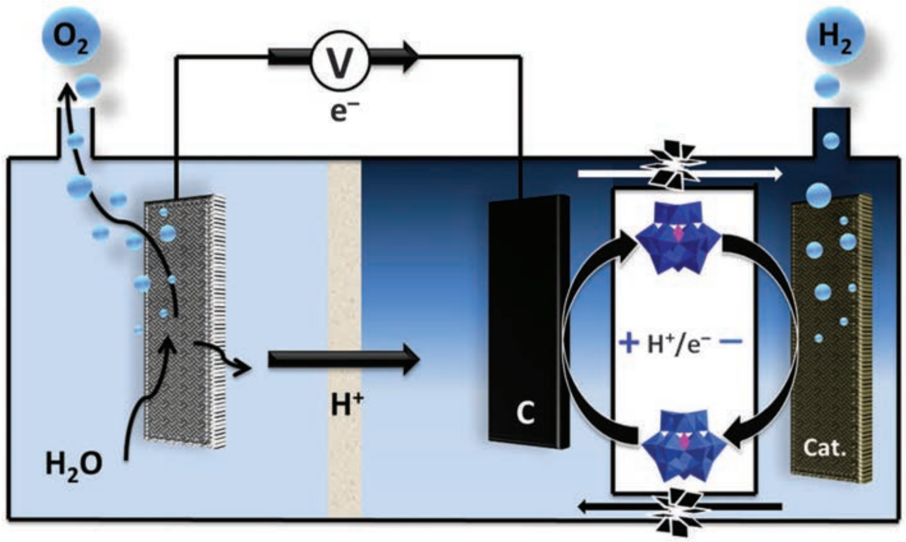

Fig. 1. A schematic of silicotungstic acid–mediated H_2 evolution from water. At the anode, H_2O is split into O_2, protons, and electrons, while the mediator is reversibly reduced and protonated at the cathode in preference to direct production of H_2. The reduced $H_6[SiW_{12}O_{40}]$ (dark blue) is then transferred to a separate chamber for H_2 evolution over a suitable catalyst and without additional energy input after two-electron reduction of the mediator to $H_6[SiW_{12}O_{40}]$.

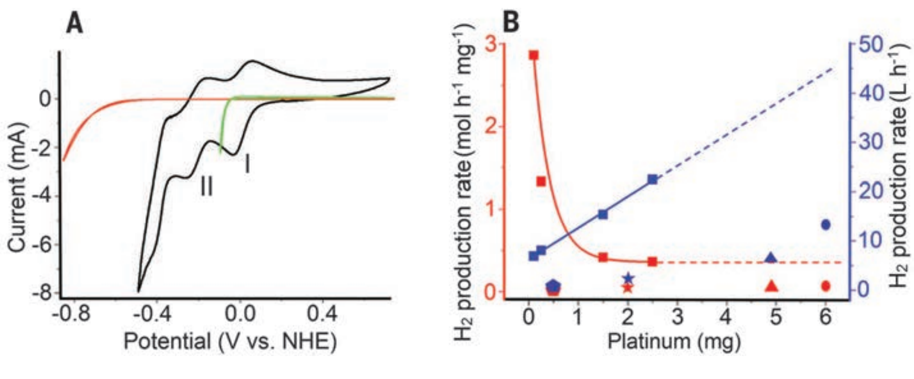

Fig. 2. Performance of silicotungstic acid as an electrochemical mediator for water splitting. (**A**) Reductive CVs under Ar and at room temperature: black, $H_4[SiW_{12}O_{40}]$ in water (0.5 M, pH 0.5), at a glassy carbon working electrode (area = 0.071 cm^2); red, 1 M H_3PO_4 (pH = 1.0) on a glassy carbon working electrode; green, 1 M H_3PO_4 (pH = 1.0) on a Pt disc working electrode (area = 0.031 cm^2). A Pt-mesh counterelectrode and Ag/AgCl reference electrode were used at a scan rate of 0.1 V s^{-1}. (**B**) Comparison of the rate of H_2 production possible using electrolysis mediated by silicotungstic acid (this work) and a selection of state-of-the-art electrolyzers from recent years. Square symbols indicate data obtained for a mediated system in this paper. Red data (left-hand *y* axis): the rate of H_2 production per milligram of Pt. Blue data (right-hand *y* axis): the absolute rate of H_2 production determined for H_2 production from $H_6[SiW_{12}O_{40}]$ (this work, squares) and the various literature electrolyzer systems. Dashed lines are provided solely as guides to the eye. Code for literature data is as follows: pentagons, reference (*30*); stars, reference (*26*); triangles, reference (*31*); dots, reference (*32*). This comparison does not include the time taken to reduce the mediator to $H_6[SiW_{12}O_{40}]$. For more details on how these metrics were obtained, see table S1.

The redox mediator investigated in this work was silicotungstic acid ($H_4[SiW_{12}O_{40}]$), the cyclic voltammogram (CV) of which on a glassy carbon electrode in aqueous solution is shown in Fig. 2A (black line). $H_4[SiW_{12}O_{40}]$ was chosen for investigation on account of its high solubility in water (up to 0.5 M), in which solvent it is a strong acid (*18*). $H_4[SiW_{12}O_{40}]$ has reversible one-electron redox waves centered at +0.01 V (wave I) and –0.22 V [wave II; all potentials are versus the normal hydrogen electrode (NHE)], the positions of which are critical to the following discussion (*18*). Also shown in Fig. 2A are reductive scans taken at a similar pH in the absence of $H_4[SiW_{12}O_{40}]$ on carbon and Pt electrodes (red and green lines, respectively). Given that the onset of H_2 evolution on Pt occurs at essentially the same potential as the first reduction of $H_4[SiW_{12}O_{40}]$, but that H_2 evolution on carbon is not appreciable above –0.6 V, we hypothesized that the reduction of $H_4[SiW_{12}O_{40}]$ at a carbon electrode at potentials slightly more positive than –0.6 V would give the two-electron reduced form ($H_6[SiW_{12}O_{40}]$) without any competing H_2 evolution. If $H_6[SiW_{12}O_{40}]$ were then exposed to Pt, it should spontaneously evolve H_2 until equilibrium between H_2 and the reduced mediator was reached, which Fig. 2A suggests will correspond to a mixture of $H_4[SiW_{12}O_{40}]$ and the one-electron reduced form, $H_5[SiW_{12}O_{40}]$.

To test this hypothesis, an airtight electrolysis cell was constructed with a Pt mesh or carbon felt anode (for water oxidation) and a carbon felt cathode (for $H_4[SiW_{12}O_{40}]$ reduction), as shown in fig. S1. Reduction of the mediator and concomitant water oxidation were performed, and the composition of the gases in the separated headspaces was monitored by gas chromatographic headspace analysis (GCHA). Full faradaic efficiency for O_2 evolution could be observed (using

Pt anodes), whereas complete two-electron reduction of the mediator could be achieved with only trace H_2 being evolved [see supplementary materials (SM) section SI-4 and figs. S2 and S3]. This two-electron reduced $H_6[SiW_{12}O_{40}]$ could then be stored without significant spontaneous H_2 evolution (<0.002% loss of H_2 per hour; fig. S3). Taken together, these data suggest that O_2 evolution and H_2 evolution can be effectively decoupled from each other using $H_4[SiW_{12}O_{40}]$, potentially allowing the O_2 produced during electrolysis to be vented to the atmosphere without the need for additional H_2 removal processes (*19*).

The two-electron reduced mediator could then be removed from the electrolysis cell and introduced into sealed reaction flasks under an atmosphere of Ar. The addition of various metal foils to this solution catalyzed H_2 evolution, with Pt exhibiting the best performance (SM section SI-5 and fig. S4A). Powdered samples of MoS_2 (*20*, *21*) and Ni_2P (*22*) were also found to be effective catalysts for H_2 evolution from $H_6[SiW_{12}O_{40}]$ (fig. S4B). However, by far the greatest rate of H_2 evolution was found when using precious metal catalysts supported on carbon. Figure 2B shows that per milligram of Pt used, the rate of H_2 production from $H_6[SiW_{12}O_{40}]$ exceeds the rate of H_2 evolution possible using a state-of-the-art PEME by a factor of 30 (red data). This more effective use of the precious metal H_2 evolution catalyst could be a result of the better dispersion of catalyst that is possible when it is not confined to an electrode.

The kinetics of H_2 evolution from solutions of $H_6[SiW_{12}O_{40}]$ as a function of time and catalyst are examined in Fig. 3A. Based on the volume of mediator solution used in these experiments, full conversion of two-electron reduced $H_6[SiW_{12}O_{40}]$ to one-electron reduced $H_5[SiW_{12}O_{40}]$ would be expected to liberate 122.4 ml of H_2, whereas complete reversion to $H_4[SiW_{12}O_{40}]$ would release 244.7 ml of H_2 (SM section SI-6). In practice, somewhat more than 122.4 ml of H_2 were liberated in under 30 min with all the catalysts examined in Fig. 3A, suggesting complete and rapid transformation of $H_6[SiW_{12}O_{40}]$ to $H_5[SiW_{12}O_{40}]$, followed by limited further conversion (10 to 36%) of $H_5[SiW_{12}O_{40}]$ to $H_4[SiW_{12}O_{40}]$ under these conditions.

Initial rates were then extrapolated to rates of H_2 produced per milligram of precious metal per hour (Table 1 and table S2), giving a maximum rate of 2861 mmol of H_2 mg^{-1} $hour^{-1}$ when using low loadings of Pt/C. The rate of H_2 evolution decays from the initial value in Fig. 3B on account of the process $H_6[SiW_{12}O_{40}] \rightarrow H_5[SiW_{12}O_{40}]$ being 80% complete within 30 s for all the Pt/C loadings shown. Hence, in a continuous flow system, it should be possible to achieve rates very similar to the initial rate measured here for as long as the flow of $H_6[SiW_{12}O_{40}]$ is maintained (the mediator could then be recycled to the cathode for recharging). Table 1 compares the rate of H_2 production by the mediator-based system with that achieved by a selection of state-of-the-art PEMEs from the recent literature (a more extensive comparison can be found in table S1). With PEMEs, the rate of H_2 production is necessarily coupled to the rate of water oxidation occurring at the anode. In a mediated electrolysis cell, the rates of water oxidation and mediator reduction are coupled, but the rate of H_2 production depends on the availability of the reduced mediator. This allows a mediated system to make more effective use of the H_2 evolution catalyst, as illustrated by Table 1. The time required to reduce the mediator is not included in the calculations for Table 1: Only the rate of H_2 production (and hence how long it would take to obtain all the H_2 from the mediator for compression and/or storage) is considered. Details on mediator reduction can be found in the

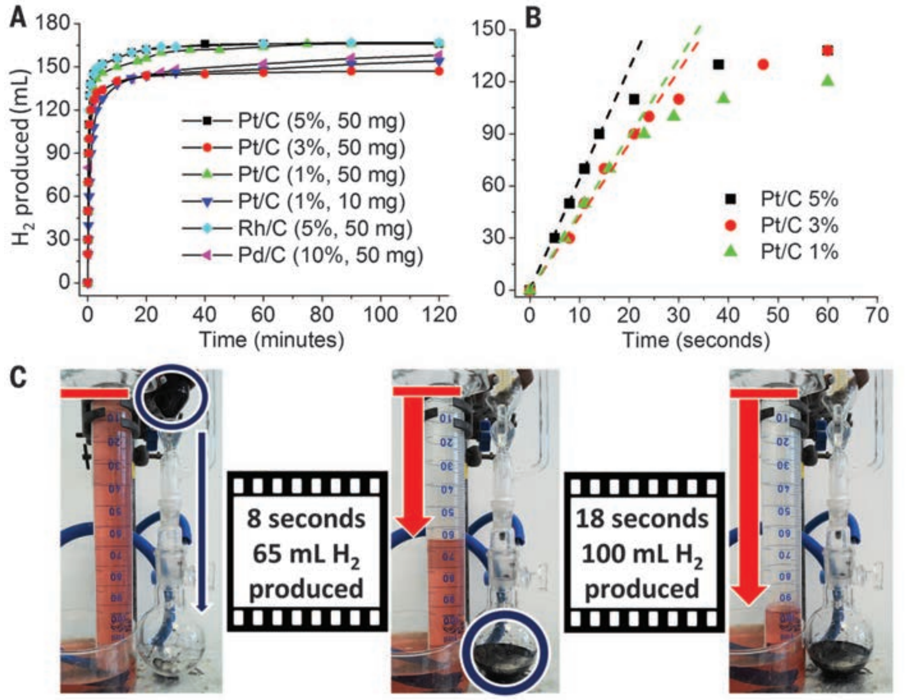

Fig. 3. Catalytic H_2 evolution from $H_6[SiW_{12}O_{40}]$ when in contact with various catalysts. (**A**) Rate of H_2 production from a 20-ml sample of 0.5 M $H_6[SiW_{12}O_{40}]$ under an Ar atmosphere. (**B**) Magnification of the first 2 min of the H_2 evolution process from $H_6[SiW_{12}O_{40}]$ in the presence of 50 mg Pt/C (5, 3, and 1 weight %). Dashed lines indicate the derived initial rates. (**C**) A typical apparatus configuration for determining volumes of H_2 evolved when $H_6[SiW_{12}O_{40}]$ was exposed to powdered catalysts. Reduced mediator in the upper flask (blue circle in left-hand photograph) is allowed to flow into the lower chamber containing catalyst (blue circle in middle photograph), and H_2 is rapidly evolved and collected (as indicated by the red arrows). A movie showing rapid H_2 evolution (movie S1) and full experimental details can be found in the supplementary materials (SM section SI-6).

Table 1. Comparison of the rate of H_2 production possible with silicotungstic acid–mediated electrolysis and a selection of leading PEMEs from the current literature. Literature values are based on the highest rate of H_2 production reported in those works. A table with more examples and a full description of how these metrics were calculated can be found in the supplementary materials.

H_2 evolution catalyst	Amount of powder/size of electrode	Total catalyst used (mg)	H_2 production rate (mmol $hour^{-1}$ mg^{-1})	Reference
Pt/C (0.5 mg of Pt cm^{-2})	9 × 100 cm^2	450	22	(*33*)
Pt/C (0.4 mg of Pt cm^{-2})	5 cm^2	2	47	(*26*)
Pt/C (0.7 mg of Pt cm^{-2})	7 cm^2	4.9	53	(*31*)
Pt/C (0.3 mg of Pt cm^{-2})	20 cm^2	6	93	(*32*)
Pd/C 10%	50 mg	5	143	This work
Rh/C 5%	50 mg	2.5	241	This work
Pt/C 5%	50 mg	2.5	368	This work
Pt/C 3%	50 mg	1.5	423	This work
Pt/C 1%	50 mg	0.5	1275	This work
Pt/C 1%	25 mg	0.25	1336	This work
Pt/C 1%	10 mg	0.1	2861	This work

supplementary materials (SM sections SI-3 and SI-7).

Next, we examined the purity of the H_2 that was produced by this silicotungstic acid–mediated method. GCHA indicated that the level of electrolysis-derived O_2 in this H_2 was below detectable limits (±0.08%; SM sections SI-4 and SI-6). Moreover, if 10% O_2 were deliberately introduced into the headspace of the vessel containing $H_6[SiW_{12}O_{40}]$, this extraneous O_2 was completely removed by reaction with $H_6[SiW_{12}O_{40}]$ (% O_2 in the headspace was only 0.04% after 30 min), ultimately producing water and reoxidized mediator (*23*) and further guaranteeing that the H_2 evolved is O_2-free (SM section SI-9 and fig. S9). This has obvious implications for electrolyzer safety, because gaseous mixtures of H_2 and O_2 on the cathode side are now precluded by the reduced mediator's rapid reaction with O_2. This reaction is spontaneous and does not require any precious metal–based recombination catalysts such as those often employed in PEMEs.

As noted earlier, a primary mode of degradation of the perfluorinated membranes used in PEMEs is attack by ROS (*12*). These ROS form in the presence of O_2, H_2, and precious metals (including the catalytic recombination layers that are designed to prevent mixtures of O_2 and H_2 forming in electrolysis product streams). Moreover, recombination of H_2 and O_2 is an exothermic process that causes local heating, damaging the membrane through mechanical means; this route is especially prevalent at Pt sites on the cathode (*24*, *25*). The use of a mediator can help to mitigate against membrane degradation in three ways. First, the amount of H_2 produced in the electrolyzer itself is vastly diminished, removing the need to purify the O_2 product stream and preventing ROS formation on the anode side of the cell. Second, on the cathode side, the reduced mediator reacts rapidly with any O_2 present to produce water, and any peroxy species that do form will do so in bulk solution far from the membrane and will themselves rapidly react with reduced mediator to form water (*23*). Finally, the catalyst is now isolated in a second chamber and is not in contact with the membrane, lessening local heating effects. Hence, using a mediator could potentially allow increased lifetimes for the membranes used in such electrolyzers relative to the life span of similar membranes in PEMEs.

The efficiency of the electrochemical process to produce O_2 from water and $H_6[SiW_{12}O_{40}]$ from $H_4[SiW_{12}O_{40}]$ was calculated and compared to equivalent systems that would produce H_2 and O_2 directly by electrolysis (SM section SI-7 and fig. S6). In comparison to a system that uses a carbon cathode to reduce protons and a Pt anode to oxidize water, the mediated system was 16% more efficient, with an overall energy efficiency of 63%. A standard electrolysis system for direct O_2 and H_2 production from water, in which both electrodes are Pt, was found to have an efficiency of 67% [which agrees well with the efficiency of room-temperature PEMEs reported in the literature (*26*)]. Hence, given the potential for lower loadings of precious metal and high initial purity of the product gases when using mediated electrolysis (and other possible technoeconomic advantages; SM section SI-12), we believe that such systems will be competitive with PEMEs in terms of cost-efficiency metrics.

The redox reactions of silicotungstic acid are summarized in fig. S10A. Starting from fully reduced $H_6[SiW_{12}O_{40}]$, H_2 evolution in the presence of a catalyst such as Pt/C is rapid, leading to the one-electron reduced species $H_5[SiW_{12}O_{40}]$. This process can be reversed by electro-reducing $H_5[SiW_{12}O_{40}]$ at a carbon cathode. Alternatively, starting from the fully oxidized species $H_4[SiW_{12}O_{40}]$, the one-electron reduced species can be accessed either by electrochemical reduction or by reaction with H_2 in the presence of a suitable catalyst such as Pt/C (SM section SI-8 and fig. S8). Likewise, if one-electron reduced $H_5[SiW_{12}O_{40}]$ is placed in a sealed reaction vessel under Ar in the presence of Pt/C, H_2 evolves slowly into the headspace, as gauged by GCHA (fig. S7). This behavior implies that there exists an equilibrium between H_2 and $H_4[SiW_{12}O_{40}]$ on one hand and the one-electron reduced mediator ($H_5[SiW_{12}O_{40}]$) on the other in the presence of catalysts such as Pt/C.

Overall faradaic efficiencies for the roundtrip process were gauged by fully reducing a sample of $H_4[SiW_{12}O_{40}]$ to $H_6[SiW_{12}O_{40}]$ with coulometry. Pt/C was then added to this $H_6[SiW_{12}O_{40}]$, and H_2 was evolved. At the cessation of spontaneous H_2 evolution, an amount of H_2 corresponding to 68% of the charge passed in reducing $H_4[SiW_{12}O_{40}]$ to $H_6[SiW_{12}O_{40}]$ was obtained. In a cyclic system, any one-electron reduced $H_5[SiW_{12}O_{40}]$ could simply be returned to the electrolyzer for re-reduction to $H_6[SiW_{12}O_{40}]$. However in this case, once H_2 evolution had ceased, the Pt/C catalyst was removed by filtration under Ar, and the resulting Pt-free mediator solution was titrated with an Fe(III) source in order to oxidize all remaining $H_5[SiW_{12}O_{40}]$ to colorless $H_4[SiW_{12}O_{40}]$ and thus ascertain the amount of $H_5[SiW_{12}O_{40}]$ still present at the cessation of H_2 evolution (SM section SI-10). This value, when combined with the electrons already accounted for by the amount of H_2 evolved, gave a faradaic yield in excess of 98% for the roundtrip $H_4[SiW_{12}O_{40}] \rightarrow H_6[SiW_{12}O_{40}] \rightarrow H_4[SiW_{12}O_{40}]$.

The stability of the mediator to several cycles of oxidation and reduction was probed both electrochemically (by comparing the charges passed in oxidizing the reducing the mediator over a series of cycles, SM section SI-13) and by comparing ultraviolet-visible spectra of fresh and cycled samples and of reduced samples that were reoxidized by exposure to air (SM section SI-14). Figure S11A shows that 98% of the charge passed in fully reducing the mediator by one electron could be retrieved by reoxidation over nine full one-electron reduction-oxidation cycles, with no apparent degradation of the mediator. Figure S11B shows the stability of the mediator to four consecutive cycles of reduction to 80% of the maximum for full two-electron reduction, followed by reoxidation to 20% of this maximum. This experiment was designed to mimic the conditions under which the mediator would have to operate in a continuous-flow system. The data in fig. S11B suggest that there is no decay in the amount of charge that can be stored in the mediator (which would signal irreversible decomposition) within these bounds over the number of cycles probed. Similarly, fig. S12, A and B, show that a sample of silicotungstic acid subjected to 20 consecutive two-electron reduction and reoxidation cycles has an ultraviolet-visible spectrum indistinguishable from that of a fresh sample of silicotungstic acid. Taken together, these data suggest that the mediator is stable to redox cycling under these conditions and that $H_4[SiW_{12}O_{40}]$ might thus be suitable as a mediator in a continuous-flow system.

Because of the high molecular weight of $H_4[SiW_{12}O_{40}]$, it does not constitute an especially effective static storage medium for H_2 (or H_2 equivalents). Clearly, lower–molecular-weight mediators, or systems capable of storing more electrons, would therefore be at a practical advantage (*15*), allowing greater buffering capacity to be built into the system and providing more flexibility with regard to the temporal separation of water oxidation and H_2 generation. We are currently pursuing the identification of such mediators, and we see great potential for optimized mediator systems to be combined with other recent breakthroughs in catalysis (*27*, *28*) and device design (*9*, *29*), facilitating the use of low-power inputs (or those subject to large fluctuations) in renewables-to-hydrogen conversion.

REFERENCES AND NOTES

1. A. Le Goff *et al*., *Science* **326**, 1384–1387 (2009).
2. N. Armaroli, V. Balzani, *ChemSusChem* **4**, 21–36 (2011).
3. U.S. Department of Energy Hydrogen Analysis Resource Center, Hydrogen Production, Worldwide Refinery Hydrogen Production Capacities (2012), http://hydrogen.pnl.gov/cocoon/morf/hydrogen/article/706.
4. J. D. Holladay, J. Hu, D. L. King, Y. Wang, *Catal. Today* **139**, 244–260 (2009).
5. F. M. Toma *et al*., *Nat. Chem.* **2**, 826–831 (2010).
6. D. Gust, T. A. Moore, A. L. Moore, *Acc. Chem. Res.* **42**, 1890–1898 (2009).
7. M. Carmo, D. L. Fritz, J. Mergel, D. Stolten, *Int. J. Hydrogen Energy* **38**, 4901–4934 (2013).
8. Y. Tachibana, L. Vayssieres, J. R. Durrant, *Nat. Photonics* **6**, 511–518 (2012).
9. S. Y. Reece *et al*., *Science* **334**, 645–648 (2011).
10. F. Barbir, *Sol. Energy* **78**, 661–669 (2005).
11. A. Berger, R. A. Segalman, J. Newman, *Environ. Sci.* **7**, 1468–1476 (2014).
12. L. Ghassemzadeh, K.-D. Kreuer, J. Maier, K. Müller, *J. Phys. Chem. C* **114**, 14635–14645 (2010).
13. V. Prabhakaran, C. G. Arges, V. Ramani, *Proc. Natl. Acad. Sci. U.S.A.* **109**, 1029–1034 (2012).
14. M. D. Symes, L. Cronin, *Nat. Chem.* **5**, 403–409 (2013).
15. B. Rausch, M. D. Symes, L. Cronin, *J. Am. Chem. Soc.* **135**, 13656–13659 (2013).
16. International Organization for Standardization, ISO 14687-2:2012, Hydrogen fuel - Product specification - Part 2: Proton exchange membrane (PEM) fuel cell applications for road vehicles, www.iso.org/iso/home/store/catalogue_ics/catalogue_detail_ics.htm?csnumber=55083 (2012).
17. N. Wiberg, E. Wiberg, A. F. Holleman, in *Inorganic Chemistry* (Academic Press, San Diego, CA, 2001), vol. 1.
18. B. Keita, L. Nadjo, *J. Electroanal. Chem.* **217**, 287–304 (1987).
19. S. A. Grigoriev *et al*., *Int. J. Hydrogen Energy* **34**, 5986–5991 (2009).
20. H. I. Karunadasa *et al*., *Science* **335**, 698–702 (2012).

21. D. Merki, S. Fierro, H. Vrubel, X. Hu, *Chem. Sci.* **2**, 1262–1267 (2011).
22. E. J. Popczun *et al.*, *J. Am. Chem. Soc.* **135**, 9267–9270 (2013).
23. A. Hiskia, E. Papaconstantinou, *Inorg. Chem.* **31**, 163–167 (1992).
24. A. B. LaConti, H. Liu, C. Mittelsteadt, R. C. McDonald, *ECS Trans.* **1**, 199–219 (2006).
25. A. S. Aricò *et al.*, *J. Appl. Electrochem.* **43**, 107–118 (2013).
26. N. Mamaca *et al.*, *Appl. Catal. B* **111–112**, 376–380 (2012).
27. T. W. Kim, K.-S. Choi, *Science* **343**, 990–994 (2014).
28. Z. Han, F. Qiu, R. Eisenberg, P. L. Holland, T. D. Krauss, *Science* **338**, 1321–1324 (2012).
29. K. S. Joya, Y. F. Joya, K. Ocakoglu, R. van de Krol, *Angew. Chem. Int. Ed.* **52**, 10426–10437 (2013).
30. J. Xu, G. Liu, J. Li, X. Wang, *Electrochim. Acta* **59**, 105–112 (2012).
31. P. Millet *et al.*, *Int. J. Hydrogen Energy* **35**, 5043–5052 (2010).
32. C. Xu, L. Ma, J. Li, W. Zhao, Z. Gan, *Int. J. Hydrogen Energy* **37**, 2985–2992 (2012).
33. S. Siracusano *et al.*, *Int. J. Hydrogen Energy* **37**, 1939–1946 (2012).

ACKNOWLEDGMENTS

This work was supported by the Engineeering and Physical Sciences Research Council (UK). L.C. thanks the Royal Society/Wolfson Foundation for a Merit Award. M.D.S. thanks the University of Glasgow for a Lord Kelvin Adam Smith Research Fellowship. We are grateful to J. Liddell (University of Glasgow) for production of the H cells used in this work. Supplementary materials are available, which include full experimental details for electrochemical procedures, GCHA, and catalytic H_2 evolution, as well as a movie showing the H_2 evolution step (movie S1). The advances presented in the work form part of a patent filing.

SUPPLEMENTARY MATERIALS

www.sciencemag.org/content/345/6202/1326/suppl/DC1
Supplementary Text Sections SI-1 to SI-14
Figs. S1 to S12
Tables S1 and S2
References (*34–42*)
Movie S1

16 June 2014; accepted 6 August 2014
10.1126/science.1257443

BLACK HOLE PHYSICS

Rapid growth of seed black holes in the early universe by supra-exponential accretion

Tal Alexander[1]* and Priyamvada Natarajan[2]

Mass accretion by black holes (BHs) is typically capped at the Eddington rate, when radiation's push balances gravity's pull. However, even exponential growth at the Eddington-limited *e*-folding time t_E ~ few × 0.01 billion years is too slow to grow stellar-mass BH seeds into the supermassive luminous quasars that are observed when the universe is 1 billion years old. We propose a dynamical mechanism that can trigger supra-exponential accretion in the early universe, when a BH seed is bound in a star cluster fed by the ubiquitous dense cold gas flows. The high gas opacity traps the accretion radiation, while the low-mass BH's random motions suppress the formation of a slowly draining accretion disk. Supra-exponential growth can thus explain the puzzling emergence of supermassive BHs that power luminous quasars so soon after the Big Bang.

Optically bright quasars powered by accretion onto black holes (BHs) are now detected at redshifts as high as $z \sim 7$, when the universe was 6% of its current age (<1 billion years) (*1*). Their luminosities imply supermassive BHs (SMBHs) with the mass of the BH ($M_\bullet$) $\gtrsim 10^9$ solar masses ($M_\odot$) (*2*). The main obstacles to assembling such SMBHs so rapidly are the low masses of the hypothesized initial seed BHs, born of first-generation (Pop III) stars, coupled with the maximal growth rate for radiatively efficient accretion, the Eddington limit (*3–5*). Proposed ways to circumvent these limitations invoke super-Eddington accretion for brief periods of time (*6*); the ab initio formation of more-massive BH seeds (*7–10*) from the direct collapse of self-gravitating pre-galactic gas disks at high redshifts (*11–14*); and the formation of a very massive star from runaway stellar mergers in a dense cluster (*15*, *16*). Discriminating between these scenarios is challenging, because seed formation redshifts ($z > 10$) are observationally inaccessible. Current data require finely tuned, continuous early BH growth and massive initial BH seeds (*17–20*). Recent results from high-resolution simulations of early star formation at $z \sim 15$ to 18 exacerbate the problem by indicating that efficient fragmentation and turbulence (*21–25*) lead to the efficient formation of stellar clusters embedded in the flow, which prevents the formation of massive seeds (>>10 $M_\odot$) by limiting the mass of their potential Pop III progenitor stars. On the other hand, theoretical and numerical results on larger scales suggest that ubiquitous dense cold gas flows (*26*) stream in along filaments and feed protogalactic cores (*27*, *28*). Adaptive mesh refinement simulations track the fate of these sites (collapsed $10^7\,M_\odot$ dark-matter halos) from 1 Mpc scale at $z \sim 21$ with resolutions as low as ~ 2×10^{-10} pc in the central regions. These simulations find isothermal density cusps that reach extreme central densities, with an average density of $\rho_\infty \gtrsim 10^{-16}$ g cm^{-3} ($\gtrsim 10^8$ cm^{-3} for pure H) on 0.1 pc scales (*29*). They also reveal a marginally unstable central gas reservoir of few × $10^5\,M_\odot$ in the inner few parsecs (*30*), where the dynamical time scale is ~10^6 years. Although these simulations are somewhat idealized, we adopt the properties of this high-density environment as the initial conditions for the model presented here.

We consider a scenario in which a low-mass Pop III remnant BH remains embedded in a nuclear star cluster fed by dense cold gas flows (*26*) (Fig. 1 and Table 1). The stars and gas are virialized in the cluster potential, and the BH is initially a test particle in equipartition with the stars. Gas within the accretion (capture) radius of the BH, $r_a = [2c^2/(c_\infty^{\,2}+v_\bullet^{\,2})]r_g$, is dynamically bound to it, where $r_g = GM_\bullet/c^2$ is the gravitational radius of the BH; c_∞ is the gas sound speed in the cold flow far from the BH, which is a measure of the depth of the cluster's gravitational potential; and $v_\bullet$ is the BH velocity relative to the gas. Gas bound to the BH inside r_a is not necessarily accreted by it. Prompt accretion requires gas to flow from r_a into the BH on a plunging trajectory with low specific angular momentum $j < j_{ISO} \simeq 4r_g c$, through the innermost stable periapse distance r_{ISO}. It is this angular momentum barrier, rather than the Eddington limit, that is the main obstacle to supra-exponential growth.

The BH is more massive than a cluster star, so $v_\bullet^{\,2} < c_\infty^{\,2}$, and the accretion flow is quasi-spherical. In the idealized case where the flow is radial and adiabatic, it is described by the Bondi solution (*31*), $\dot{M}_B = (\pi/\sqrt{2})r_a^2\rho_\infty c_\infty$ (adiabatic index $\Gamma = 4/3$ assumed), which can be written compactly in terms of $\mu = M_\bullet/M_i$, where M_i is the initial BH mass, as $\dot{\mu} = \mu^2/t_B$, with time scale $t_B = c_\infty^{\,3}/\,2^{3/2}\pi G^2 M_i \rho_\infty$. The stronger-than-linear dependence of the accretion rate on the BH mass leads to a solution that diverges supra-exponentially in a finite time t_B as $\mu(t) = 1/(1 - t/t_B)$. Physical flows, where gravitational energy is released as radiation, are not strictly adiabatic. As the mass accretion rate grows, the local luminosity can far exceed the Eddington luminosity $L_E = 4\pi cGM_\bullet/\kappa = \dot{M}_E c^2$ (κ is the gas opacity), for which radiation flux pressure balances gravity. However, radiation produced inside the photon-trapping radius $r_\gamma \sim (\dot{M}/\dot{M}_E)r_g$ is carried with the flow into the BH, because the local optical depth $\tau(r) \sim \kappa\rho(r)r$ makes photon diffusion outward slower than accretion inward (*32*) [which is a manifestation of the $\mathcal{O}(v/c)$ effect of relativistic beaming (*33*)]. The luminosity L_∞ that escapes to infinity from $r \gtrsim r_\gamma$ translates to a lowered radiative efficiency $\eta_\gamma = L_\infty/\dot{M}c^2 \sim \min(r_g/r_\gamma, r_g/r_{ISO})$, so it does not exceed ~L_E, thereby allowing supra-exponential Bondi mass accretion rates (*34*). Detailed calculations show that $L_\infty \lesssim 0.6\,L_E$ (*35*).

[1]Department of Particle Physics and Astrophysics, Weizmann Institute of Science, Rehovot 76100, Israel. [2]Department of Astronomy, Yale University, 260 Whitney Avenue, New Haven, CT 06511, USA.
*Corresponding author. E-mail: tal.alexander@weizmann.ac.il